Check for updates

Batteries & Supercaps

Articles
doi.org/10.1002/batt.201900202

Chemistry Europe
European Chemical
Societies Publishing

Effect of Crystal Structure and Morphology on Na_3V_2 $(PO_4)_2F_3$ Performances for Na-Ion Batteries

Ayan Mukherjee+,[a, b] Tali Sharabani+,[a, b] Rosy Sharma,[a, b] Sivan Okashy,[a, b] and
Malachi Noked*[a, b]

Na-ion batteries (SIB) are considered promising systems for energy storage devices, however diversity of available cathode materials is lower compared to lithium ion batteries. Recently, $Na_3V_2(PO_4)_2F_3$ (NVPF) has been demonstrated as promising cathode material for SIB owing to high specific capacity and electrochemical reversibility. However, most of reports demonstrates capacities lower than theoretical value and optimization of electrochemical performances by controlled morphology and crystal structure was not demonstrated yet. Here, we demonstrate a scalable synthesis strategy to tailor the crystal structure and morphology of NVPF and showed that our approach enables to optimize the Na^+ ion accommodation, diffusion and stability. A flower morphology (NVPF-F) crystalizes in tetragonal structure, demonstrates discharge capacity of 109.5 mA.h.g^{-1} and 98.1% columbic efficiency whereas a hollow spherical morphology (NVPF-S) with orthorhombic structure exhibits discharge capacity of 124.8 mA.h.g^{-1} (very close to theoretical value) and 99.5% columbic efficiency. The observed discharge capacity for NVPF-S is highest reported value which is ascribed due to stable crystal structure and monodispersed morphology. Long term stability with negligible capacity loss is demonstrated over 550 cycles. Our findings shed light on importance of crystal structure and morphology of NVPF on electrochemical response, and realization as cathode material for SIB.

1. Introduction

Secondary battery systems are a promising technology for large scale energy storage due to its economic viability, high round trip efficiency, and ease of maintenance.[1–5] Lithium ion batteries (LIB), since their commercialization in 1990 conquered the portable electronic market[6] and brought it to a new age due to its longevity and energy storage capabilities. However, the limited supply, and heavy demand of lithium, and the relevant transition oxides (e.g. Co) strongly effect the price of electronic devices powered by LIB.[7–9] For large energy storage units, there is a dire need for cheaper active materials, even on the account of gravimetric\volumetric energy densities. In order to reduce the cost without compromising the round trip efficiency, the search for alternatives stepped to sodium, which is the fourth most abundant element in earth crust .[10] Sodium ion batteries (SIB), however, possess a less negative standard reduction potential for the Na^+_{aq}/Na (-2.7 V vs SHE) as compared to Li^+_{aq}/Li (-3.04 V vs SHE), larger ionic radius for Na^+ (1.07 Å) as compared to Li^+ (0.76 Å), which cause long term structural instability, lower gravimetric capacity, lower energy density and slow ion diffusivity (due to sluggish sodium mobility).[11–13] In order to optimize SIB performances and to overcome part of these challenges, the scientific community focused on design of new electrode materials (EMs) and precise controlled architecture of EMs.[14–21] These EMs were engineered to facilitate highly reversible sodiation/desodiation with high kinetics and energy density.

Among various candidates, layered transition metal oxides,[22,23] transition metal sulfides[24,25] and fluorides[16,26] were extensively studied. Prussian blue analogues and polymers have attracted considerable attention globally in terms of higher specific capacity but delivers poor cycling stability.[22,27] Recently, a polyanionic compound $(Na_3V_2(PO_4)_3)$ with a Na super ionic conductor (NASICON) structure possessing stable 3D open framework for the rapid Na-ion migration attracted tremendous attention in the search of cathode materials for SIBs as it facilitated stable structure, high voltage profile, excellent reversible capacity and cycling performance.[28–33] When one of the $(PO4)^{-3}$ ion in $Na_3V_2(PO_4)_3$ is substituted by three F^- ions, a typical fluorophosphate, $Na_3V_2(PO_4)_2F_3$ (NVPF) can be obtained with higher theoretical energy density (about 507 W.h. kg^{-1}), average potential (3.95 V) and theoretical capacity (128 mA.h.g^{-1}) than that of $Na_3V_2(PO_4)_3$. The NVPF structure consist of $V_2O_8F_3$ bi-octahedra connected to PO_4 tetrahedra periodically which endows with large tunnels along the [110] and [110] crystallographic directions and the open 3D cage produces large interstitial spaces for facilitating Na^+ diffusion.[34]

[a] Dr. A. Mukherjee,+ T. Sharabani,+ Dr. R. Sharma, Dr. S. Okashy,
Dr. M. Noked
Department of Chemistry
Bar Ilan University, Ramat Gan, 5290002, Israel
E-mail: malachi.noked@biu.ac.il

[b] Dr. A. Mukherjee,+ T. Sharabani,+ Dr. R. Sharma, Dr. S. Okashy, Dr. M. Noked
Bar-Ilan Institute of Nanotechnology and Advanced Materials
Ramat Gan, Israel

[+] These authors contributed equally to this work.

Supporting information for this article is available on the WWW under https://doi.org/10.1002/batt.201900202

Despite the high potential of NVPF, limited reversible capacity, poor electronic conductivity, low sodium-ion diffusivity and cycling stability hinders its realization as cathode in SIB. To address these issues, rational designing of the electrode material with control over the morphology and crystal structure is essential to tailor the specific capacity, cycling performance and energy density. Recently, few studies focused on the synthesis of different morphologies of NVPF microstructures by hydro/(solvo)thermal and conventional solid state reaction approaches that enabled to get controllable microstructure, and cation doping. These modifications and efforts ended in improving the performance and stability to some extent .[35–41] Previous studies suggest that the electronic conductivity of NVPF can be improved greatly from its pristine counterpart by suitably coating with carbon,[15] CMK-3,[42] graphene,[43] RuO_2,[44] carbon-polytetrahydrofuran[45] or compositing with MWCNT.[46,47] However, the volume expansion during repeated Na^+ ion intercalation/deintercalation accounted for wobbly interface between NVPF and coated material and lead to separation of the coating in long cycling which hinders its cycling stability and rate capability. So, rational designing of pristine NVPF with controlled crystal engineering is essential which can deliver cycling performance similar or even better than reported coated or composite NVPF electrode till now to meet the requirement of commercial SIB. Further adopting the surface modification, coating and compositing strategies might account for some improvement in the stability of NVPF. Also, the relationship between morphology and crystal structure and EMs performance still remains unexplored in NVPF and demands close attention for optimization and realization of this material.

In the present work, a unique synthesis approach enabled to tailor the crystal structure and morphology of NVPF. We show how our approach, enabled to optimize the electrochemical response in terms of sodium accommodation capacity and diffusivity in NVPF which is without any support and coating. Specifically, a facile one step solvothermal route is demonstrated for synthesis of NVPF in two different microstructures; (1) micro-hollow-spherical (MHS) morphology consist of sub-micron plates which crystallizes in orthorhombic structure and (2) micro-flower (MF) morphology composed of sub-micron flakes which crystallizes in tetragonal structure. Both the architecture exhibit excellent electrochemical performance as cathodes for SIBs but the MHS displays superior discharge capacity (124.8 mA.h.g^{-1}), rate performance, stability and columbic efficiency (99.5%) than the MF morphology and to any previously reported NVPF. We show that the 3D open structure in orthorhombic phase (in MHS EM) facilitate facile Na intercalation/deintercalation and faster kinetics without noticeable degradation. We believe that our orthorhombic NVPF with MHS morphology would be the most promising EM in SIB which could be improved further through selective surface modification, coating and compositing strategies in near future.

Experimental Section

Synthesis

All the precursors were procured from Sigma-Aldrich and used without further purification.

Synthesis of NVPF flowers

In a typical synthesis, 157.30 mg VCl_3, 359.94 mg $NaH_2PO_4.2H_2O$ and 70.12 mg NaF were dissolved in 5 ml ultra-pure water (MilliQ 18.2 MΩ) and stirred for 6 h. The above solution was sealed in a 30 ml Teflon lined stainless steel autoclave and kept in a muffle furnace at 200 °C for 12 h at a heating rate of 5 °C min^{-1}. After the reaction, the autoclave was allowed to cool naturally inside the furnace to room temperature. The product was centrifuged and washed repeatedly with ultrapure water and ethanol to remove the aqueous and alcohol soluble inorganic impurities completely and dried in a hot-air oven at 60 °C for 12 h to obtain the NVPF flower (NVPF-F). The formation of microflower is achieved by the aggregation and densification of nanoflakes allowing significant utilization of active material.

Synthesis of NVPF hollow microsphere

In order to synthesize NVPF hollow microspheres (NVPF-S), 167.96 mg NaF, 719.88 mg $NaH_2PO_4.2H_2O$ were dissolved in mixed solution of 6 ml H_2O and 24 ml tetraethylene glycol and stirred vigorously for 18 h. To the above solution, 233.96 mg NH_4VO_3 and 768.48 mg citric acid were added and stirred for 6 h so that all the precursors were dissolved completely. The mixed solution was autoclaved in a 50 ml Teflon lined stainless steel autoclave and kept in a muffle furnace at 200 °C for 10 h at a heating rate of 8 °C min^{-1}. The rest of the procedure is same as that of NVPF-F. The formation of hollow microsphere is governed by the oriented aggregation and densification of nanoparticles and nanoplates assembly through Oswald ripening, which allows better utilization of the active material.

Characterization

Physical characterization

The x-ray diffraction (XRD) measurements was carried in a Bruker D8 Advanced X-ray diffractometer using Cu Kα radiation (λ = 1.5414 Å) within the 2θ range from 10° to 80° to study the crystal structure of the prepared samples. The surface morphology was analyzed by environmental scanning electron microscope (SEM, Quanta 2000, from FEI) operating at 3 keV, and high resolution scanning electron microscope (HRSEM, FEI, Magellan 400 L) at the voltage of 5 kV and current of 0.4nA. The High resolution transmission electron microscope (HR-TEM, JEM 2100, JEOL, Accelerating Voltage 200 kV, Gatan USC 4000 4×4k camera) images were taken to study the morphology and crystallinity of the prepared samples. TEM samples were prepared by grinding and dispersing the powder samples in ultra-pure water and cast on a lacey carbon-coated Cu grids. The specific surface area of NVPF powder was measured using the NOVA 3200E Quantachrome Brunauer-Emmett-Teller (BET) instrument. The final composition of NVPF was measured in Inductively coupled plasma atomic emission spectrometry (ICP-AES) technique with an Ultima-2 spectrometer (JobinYvon Horiba). X-ray photoelectron spectroscopy (XPS) study was done by Thermo Scientific Nexsa spectrometer.

Electrode preparation

Composite electrodes were prepared by mixing 70% of the active material (NVPF), 20% of Super P carbon black and 10% of poly (vinylidene fluoride) (PVDF) in N-methyl-2-pyrrolidone (NMP). Mixing of the composite electrode was carried out using a Thinky mixer (ARV-310/ARV-310LED) at 2000 rpm, 30 kPa for 3 minutes. The 60-micron thick layer of the prepared slurry was then coated on a clean and polished Al foil using doctors blade and dried for overnight at 100 °C. After rolling, 14 mm of the electrode was punched and dried overnight under vacuum at 120 °C.

Electrochemical measurements

NVPF electrodes (ø 14 mm) were assembled in a two-electrode cells configuration using standard coin-type cells versus Na metal (ø 14 mm) counter electrodes in electrolyte solution of 45 μL of $NaPF_6$ (1 M) in propylene carbonate (PC) with 2% of fluoroethylene carbonate (FEC). The cell preparation was done in a glovebox under Argon atmosphere. Two polypropylene separators (ø 18 mm) were placed between NVPF and Na electrodes. The cell was taken out of the glovebox for electrochemical measurements, which was tested with galvanostatic discharge-charge cycling at 35 °C (Bio-logic Science instruments) in a potential window of 2.5–4.3 V. All the currents were normalized by mass of the active material in the study. The post mortem study was done by disassembling the cells inside the glovebox and rinsing the electrodes with dimethyl carbonate (DMC) and dried for overnight.

2. Results and Discussion

The X-ray diffraction (XRD) patterns of NVPF-F and NVPF-S are shown in Figure 1a and b respectively. These patterns match well (#01-089-8485) without the presence of any other phases. The structural and microstructural parameters are obtained by refining the powder XRD data using Rietveld powder structure refinement method. The experimental data is simulated with respect to the standard pattern while the background is fitted with a polynomial of degree 4 till convergence (goodness of fitting (χ^2) ~ 1).[48] All the diffraction peaks of NVPF-F indexed into tetragonal crystal system with $P4_2/mnm$ space group, $a = b = 9.047$ Å, $c = 10.7050$ Å[37,40] while the diffraction peaks of NVPF-S indexed into orthorhombic crystal system with $Pnnm$ space group, $a = 9.1665$ Å, $b = 9.1976$ Å, $c = 10.9237$ Å.[49] By extracting the parameters of Rietveld refinement (Table S1) and looking into the structure deeply, it is observed that both NVPF-F (Figure S1a) and NVPF-S (Figure S1b) exhibits an open 3D bridged structure where the $V_2O_8F_3$ octahedral unit is connected by PO_4 tetrahedral unit, consistent with previous report.[34] However, the Na occupies two interstitial position (Na1 and Na2) in NVPF-F along the [100] and [010] directions from each bioctahedral unit as shown in Figure 1c whereas the NVPF-S exhibit Na3 site together with Na1 and Na2 along the [110] direction shown in Figure 1d. The $Pnnm$ phase is the broken symmetry structure of $P4_2mnm$, where the Na$^+$ ions are distributed anisotropically along the [110] direction.[49] The
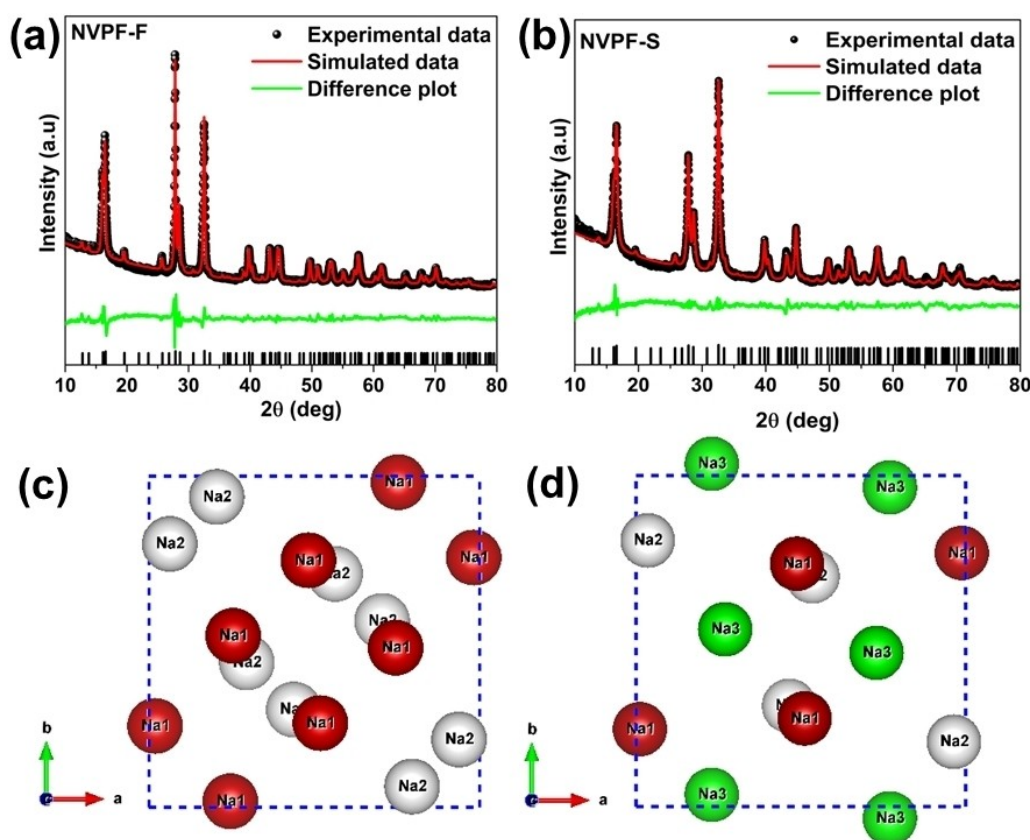

Figure 1. XRD pattern of a) NVPF-F, b) NVPF-S. Position of Na ion in the unit cell in c) NVPF-F, d) NVPF-S.

position of Na$^+$ ions are shifted from the minimum symmetry position due to electrostatic repulsion between Na–Na,[50] hence, available for intercalation/de-intercalation more easily than $P4_2/mnm$.

The morphology of NVPF-F and NVPF-S is depicted by SEM image, presented in Figure 2a–b, c–d, respectively. The NVPF-F shows flower-like morphology with an average diameter of 3 μm composed of several thin flakes, while the NVPF-S shows uniform hollow spherical morphology with an average diameter of 2 μm composed of sub-micron plates. The formation of both NVPF-F and NVPF-S is governed by oriented aggregation of nanoparticles assembly followed by Oswald ripening.[51,52] Further, in order to gain dipper understanding of the materials architecture, HRTEM images were also collected. Typical TEM images of NVPF-F and NVPF-S are shown in Figure 3a and b respectively. It is clear that the assembly of nanoparticles and nanoflakes form the flower-like morphology of diameter 3 μm in NVPF-F. The corresponding HRTEM image shown in Figure S2a validates the polycrystalline nature and matches with (220) plane of NVPF. The selected area electron diffraction (SAED) pattern taken from a portion of Figure 3a as shown in Figure S2b, further confirm the phase purity and polycrystalline nature of NVPF-F. The TEM image of monodispersed hollow microspheres of diameter 2 μm is obtained to be of sub-micron

plate assembly. The HRTEM and SAED pattern shown in Figure 2c and d respectively confirms the phase purity and polycrystalline nature of NVPF-S.

Further in order to determine the exact composition and valance state of vanadium ion in our NVPF, XPS spectra is shown in Figure S3. The V2p and O1s fine structure is taken to determine the exact valance state of vanadium. The O1s peak for NVPF-F and NVPF-S is positioned at 530.0 eV and V2p$_{3/2}$ and V2p$_{1/2}$ peaks are positioned 515.5 eV and 522.8 for both NVPF-F and NVPF-S as shown in Figure S3a and c respectively confirming the +3 oxidation of vanadium and Na$_3$V$_2^{III}$(PO$_4$)$_2$F$_3$ composition.[53] The XPS full spectra for NVPF-F (Figure S3b) and NVPF-S (Figure S3d) indicates the presence of Na, V, P, O and F similar to previous reports.[39] The stoichiometry is further studied through the ICP-AES measurement which shows that the molar ratio Na:V is 1.5 validates the composition of Na$_3$V$_2^{III}$(PO$_4$)$_2$F$_3$.

The specific surface area and pore size distribution of NVPF-F and NVPF-S is shown in Figure 4. It is observed that both NVPF-F and NVPF-S exhibit type-IV isothermal adsorption-desorption curves. The specific surface area calculated according to the Brunauer-Emmett-Teller (BET) model for NVPF-F and NVPF-S is 35 m^2.g^{-1} and 31 m^2.g^{-1} respectively. The Barrett-Joyner-Halenda (BJH) pore size distribution curve (Figure 4b)
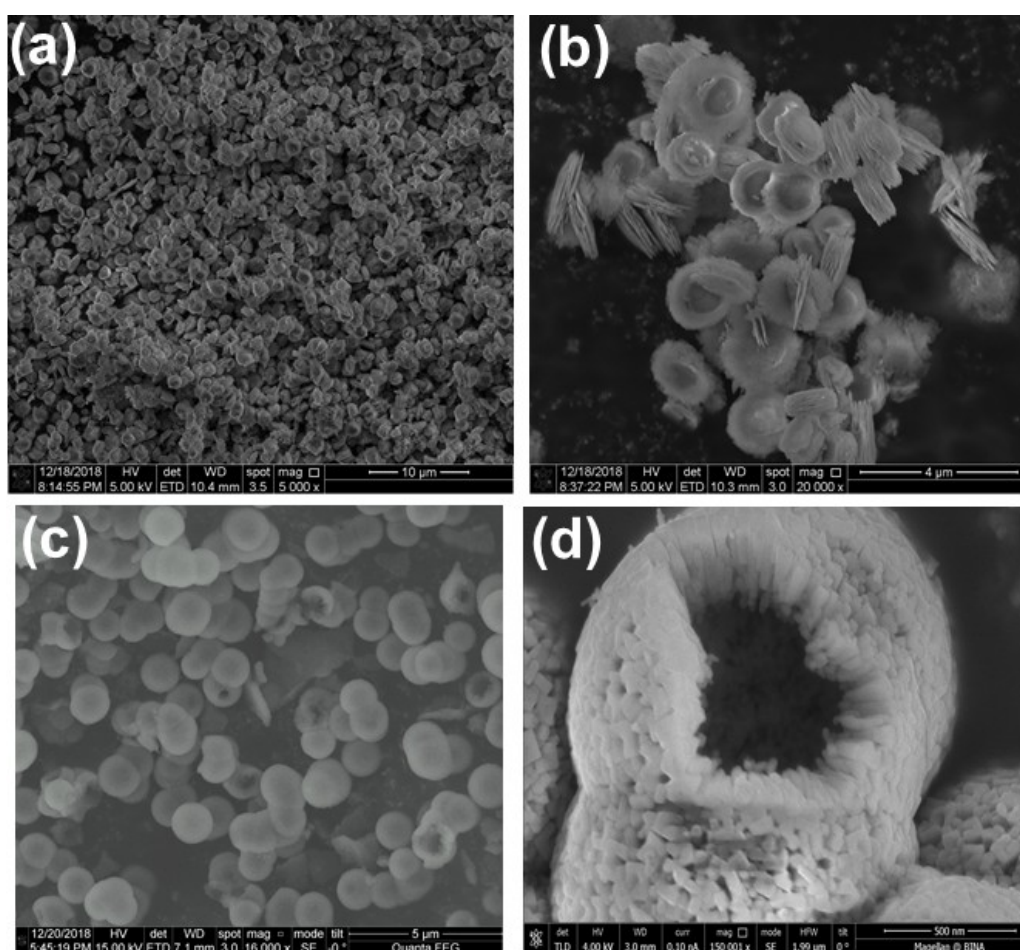

Figure 2. a), b) Low and high magnification images of NVPF-F. c), d) Low and high magnification images of NVPF-S.
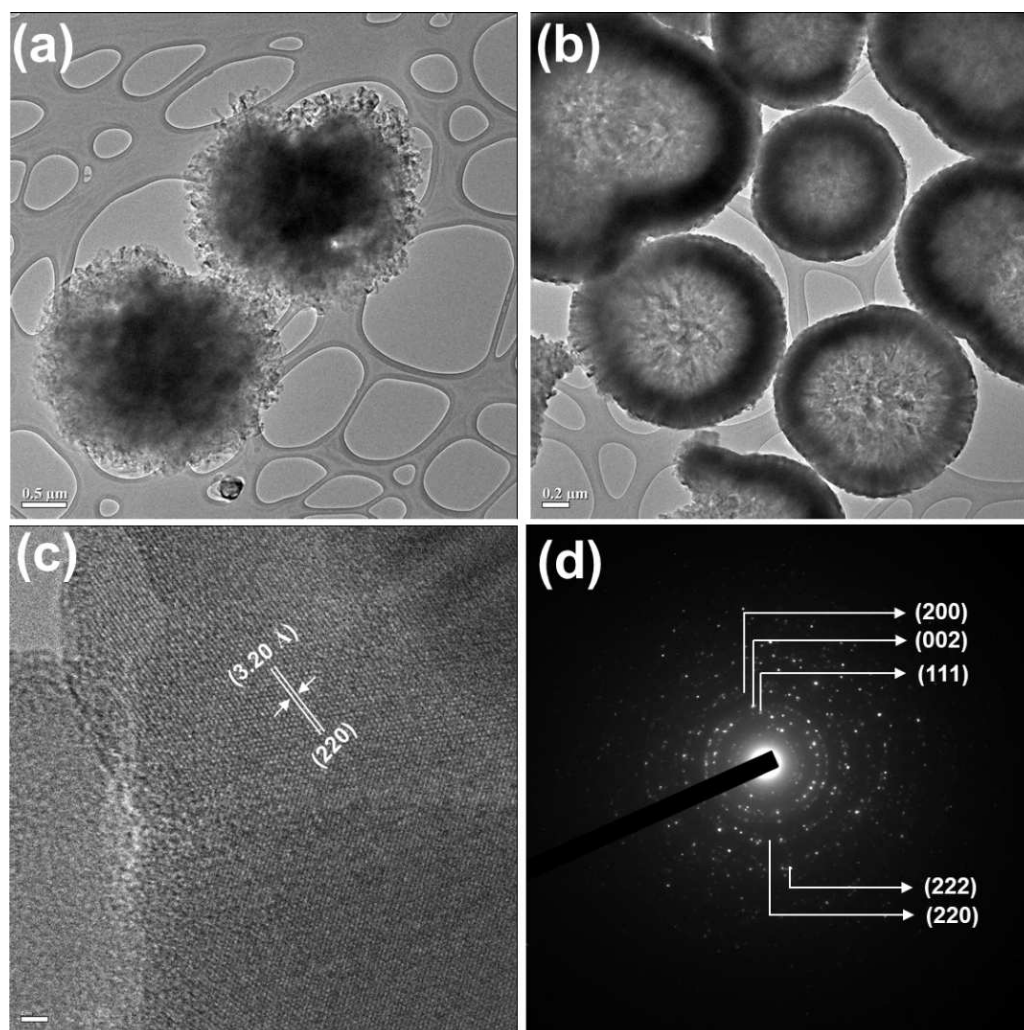
Figure 3. TEM image of a) NVPF-F b) NVPF-S, c) HRTEM and d) SAD pattern of NVPF-S.

reveals that the majority pore size in NVPF-F and NVPF-S is about 3.2 nm and 4.5 nm respectively.

The electrochemical performance of the electrodes is tested in potentials widow of 2.5 V to 4.3 V. Further, the 5th and the 40th cycles of NVPF-F and NVPF-S are shown in Figure 5a and b, respectively. The initial discharge capacity in NVPF-F and NVPF-S reaches 109.5 and 124.8 mA.h.g^{-1} respectively. Considering that specific capacity of 64 mA.h.g^{-1} is achieved on insertion/extraction of one Na$^+$ ion,[50,54] the NVPF-F and NVPF-S forms Na$_{2.71}$V$_2$(PO$_4$)$_2$F$_3$ and Na$_{2.95}$V$_2$(PO$_4$)$_2$F$_3$ upon discharge, respectively.

The rate performance of NVPF-F and NVPF-S as shown in Figure 5c reveals that as the normalized current density changes from 10 mA.g^{-1} to 30 mA.g^{-1}, 50 mA.g^{-1}, 80 mA.g^{-1} and back to 10 mA.g^{-1}, both the NVPF-F and NVPF-S exhibit excellent reversible capacities. Specifically, NVPF-F exhibit capacity of 109.5 mA.h.g^{-1}, 103.1 mA.h.g^{-1}, 98.1 mA.h.g^{-1} and 93.7 mA.h.g^{-1} on current densities of 10 mA.g^{-1} to 80 mA.g^{-1} respectively and recovered 103.5 mA.h.g^{-1} on 10 mA.g^{-1}, whereas NVPF-S exhibit capacity of 124.8 mA.h.g^{-1}, 118 mA.h.g^{-1}, 110.8 mA.h.g^{-1}, and 102.8 mA.h.g^{-1} on the same current

densities and recovered 122.1 mA.h.g^{-1} on 10 mA.g^{-1}, suggesting the superior recovery capability of NVPF-S than NVPF-F. Further, following the rate performance both NVPF-F and NVPF-S undergo cycling for another 100 cycle at 50 mA.g^{-1} as shown in Figure 5d. It is observed that with the long term electrochemical cycling the NVPF-F and NVPF-S recovered discharge capacities of 86.05 mA.h.g^{-1} and 107.35 mA.h.g^{-1} respectively. The improved performance in NVPF-S ascribed to the spherical morphology and orthorhombic structure which eventually dictates the electrochemical functionality.

The galvanostatic charge/discharge profiles of NVPF-F and NVPF-S at current rate of 80 mA.g^{-1} are shown in Figure 6a and b respectively. All the capacities are estimated by considering the mass of NVPF only. Both the NVPF-F and NVPF-S exhibits two clear charge/discharge plateaus, which corresponds to Na$^+$ ion extraction and insertion from Na (2) and Na (1) sites respectively into the NVPF matrix.[50,55,56] The structure observed from the XRD study suggests that Na$^+$ ion occupying both the Na (1) site with full occupancy and Na (2) sites with half occupancy. Moreover, the Na$^+$ ions at Na (2) site are reported to be less stable and can be easily extracted at lower potential
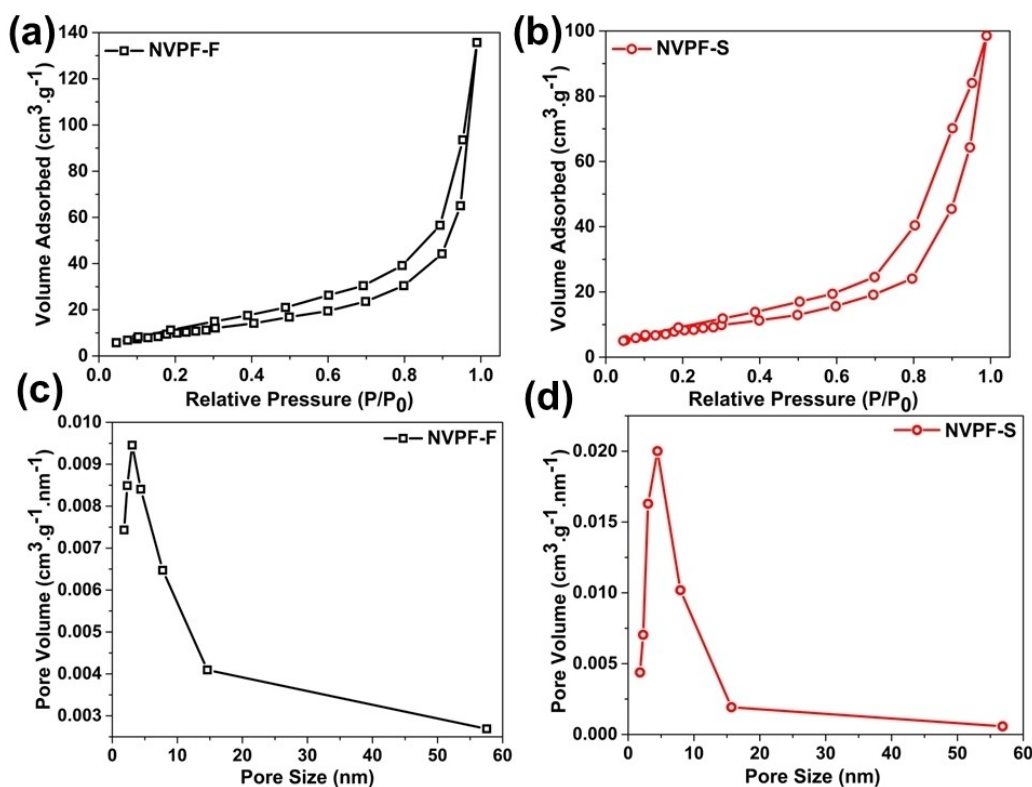
Figure 4. N$_2$ adsorption-desorption isotherm of a) NVPF-F, b) NVPF-S. Pore size distribution of c) NVPF-F, d) NVPF-S
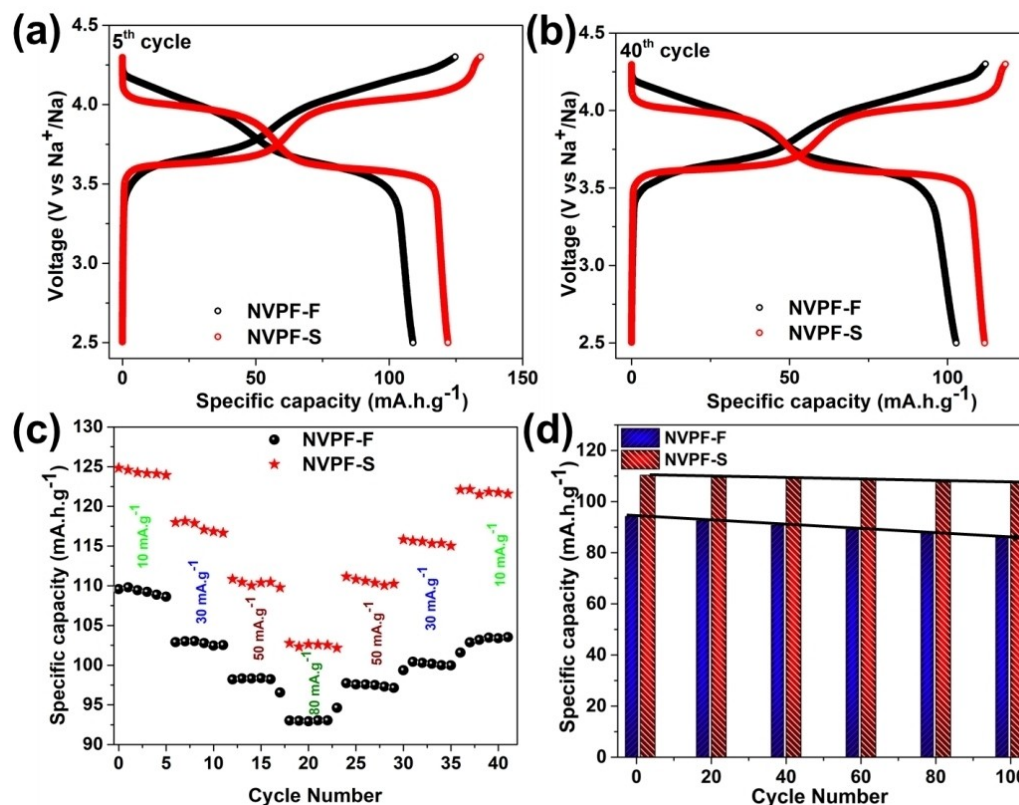

Figure 5. a) 1st cycle, b) 2nd cycle, c) rate capability of NVPF-F and NVPF-S. d) Performance of the electrodes after rate capability
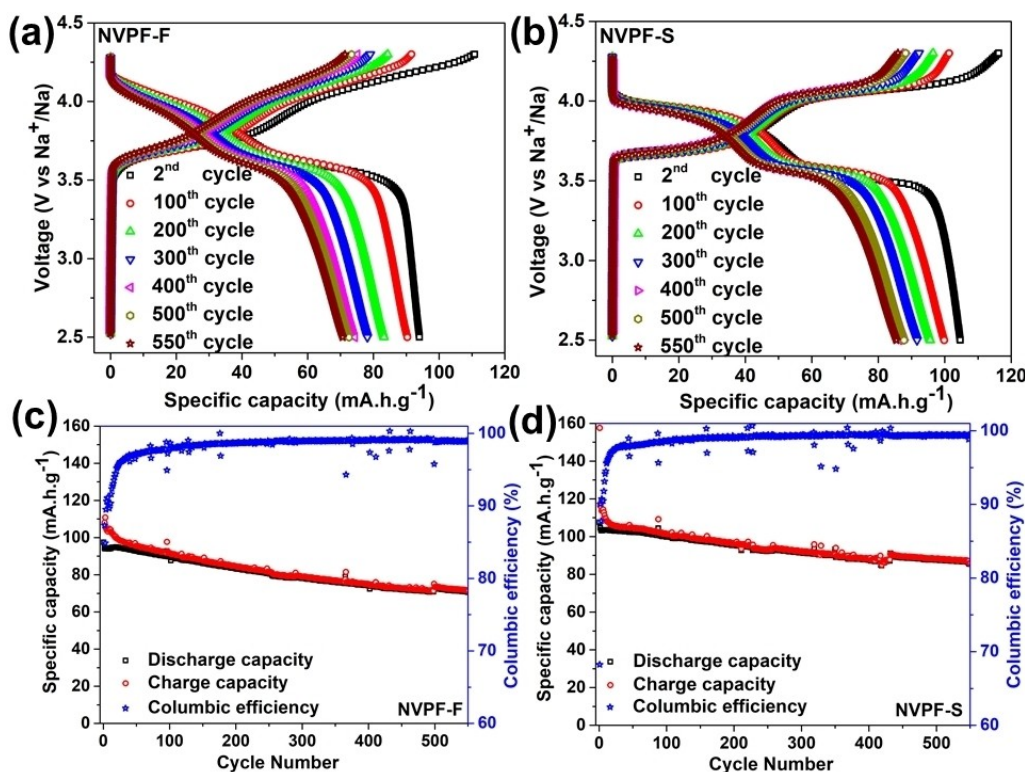
Figure 6. Charge-discharge performance of a) NVPF-F, b) NVPF-S. Cycling performance of c) NVPF-F, d) NVPF-S.

than the Na^+ ions at Na (1) site.[50] The extraction of first Na^+ ion from the Na (2) site leads to a structural instability due to short Na—Na distances (2.92 Å) of both Na (1) sites which is compensated by the reorganization of left over Na ions to a stable configuration.[36] After the reorganization of residual Na ions, the second Na^+ ion could be extracted at higher potential for stabilizing the structure giving rise to a plateau at 4.15 V. The two step intercalation during discharge for insertion of two Na ions into the NVPF structure is established through the voltage plateaus at 4.02 V and 3.60 V. The voltage plateaus for NVPF-S are much more distinct and flat than NVPF-F, suggesting more facile and pronounced kinetics for Na ion intercalation and de-intercalation due to the 3D open architecture (Figure S1), larger volume of unit cell to accommodate more Na^+ ion (Table S1) and availability of Na (3) site in *Pnnm* space group (Figure 1d). The cycling performance of both NVPF-F and NVPF-S at current density of 80 mA.g^{-1} over 550 cycles is shown in Figure 6c and d respectively. The NVPF-F managed to retain discharge capacity and columbic efficiency of 76 mA.h. g^{-1} and 98.1% respectively, whereas NVPF-S retained 90 mA.h. g^{-1} and 99.5% respectively. Further, the NVPF-S cathode is performed at high current rate (406 mA.g^{-1} ~3.1 C) and exhibit discharge capacity of 73.5 mA.h.g^{-1} with columbic efficiency of 98.5% for 150 cycles as shown in Figure S4 demonstrating its excellent performance and stability as compared to state-of-art NVPF reported (Table S2).

The kinetics of the NVPF-F and NVPF-S electrode is further studied by measuring the dQ/dV for the 2nd potentiostatic cycle at 10 mA.g^{-1} as shown in Figure S5. It is observed that the

NVPF-S exhibit sharp and clear oxidation/reduction peaks as compared to NVPF-F confirming the facilitated Na^+ ion diffusion and superior stability. Although, NVPF-F exhibit high surface area than NVPF-S, a larger gap in the oxidation/reduction potential of NVPF-F is observed than the NVPF-S, might be due to minor electrolyte decomposition and other side reactions. The cyclic voltammetry (CV) curve of NVPF-S is shown in Figure S6 at 0.1 mV.s^{-1} clearly visualizes the two redox couple positioned at 4.1 V/3.9 V and 3.7 V/3.5 V which corroborates with previous studies for NVPF.[39,46] Putting our findings in perspective, shed the light on the importance of crystal structure and morphology of the active material, it is clear that the NVPF-S material exhibit a superior electrochemical response and long term stability due to the facilitated diffusion of Na^+ ion and stabilized morphology and crystal structure.

Post mortem structural and morphological study of the electrode are presented in Figure S7 and S8. Both NVPF-F and NVPF-S retain their initial crystal structure with an obvious shifting of diffraction peaks towards lower angle. The shifting of the diffraction peaks due to repeated Na^+ ion intercalation/de-intercalation and increase in inter planar spacing. The morphology of both the electrodes is well maintained as compared to the pristine electrodes except for minor cracking. The cracks appear due to the crude electrochemical step but the overall morphology is still preserved and distinct suggesting excellent stability and corrosion resistance to the electrodes in the electrolyte.

Batteries & Supercaps

Articles
doi.org/10.1002/batt.201900202

Chemistry Europe
European Chemical
Societies Publishing

The superior performance of NVPF-S (charge/discharge capacities, rate performance, cyclability) without any coating (C, CNT, RGO) or doping (Mn, Al) in Na-ion battery govern its prominence in high voltage battery, which attributed to the negligible volume expansion, structural and morphological stability upon long and crude cycling leading to facile Na-ion diffusion, which opens up the possibility in the field for further improvement through coating and doping.

3. Conclusions

In summary, we demonstrate a facile strategic synthesis approach to tailor the crystal structure and morphology of NVPF. We synthesized two different morphologies and crystal structure of NVPF: (1) a flower morphology consist of nano flakes which crystalizes in tetragonal structure and (2) micro hollow spherical morphology consist of nanoplates crystalizes in orthorhombic structure. The electrochemical cycling results demonstrate that the flower morphology exhibit discharge capacity of 109.5 mA.h.g^{-1} at 10 mA.g^{-1} and 98.1% columbic efficiency even at 80 mA.g^{-1} whereas the micro hollow spherical morphology exhibit discharge capacity of 124.8 mA.h.g^{-1} at 10 mA.g^{-1} and 99.5% columbic efficiency at 80 mA.g^{-1}. Both the morphologies exhibit excellent capacity retention over 550 cycles. The voltage plateaus suggest that the MHS morphology exhibit easy and pronounces Na$^+$ ion diffusion during deintercalation/intercalation as compared to flower morphology which is accounted for the orthorhombic structure. Further the post mortem structural and morphological studies suggested that electrodes remain invariant during Na$^+$ ion diffusion in different current rates validate the stability preciously.

Conflict of Interest

The authors declare no conflict of interest.

Keywords: sodium-ion battery · cathode material · Na$_3$V$_2$(PO$_4$)$_2$F$_3$ · energy storage

[1] H. Pan, Y. S. Hu, L. Chen, *Energy Environ. Sci.* **2013**, *6*, 2338.
[2] D. Bruce, K. Haresh, T. Jean-Marie, *Science* **2011**, *334*, 928.
[3] M. N. E. Evenstein, Rosy, S. Haber, H. Sclar, L. Houben, K. Leung, M. Leskes, *Energy Storage Mater.* **2018**, 1.
[4] M. Salama, R. Attias, B. Hirsch, R. Yemini, Y. Gofer, M. Noked, D. Aurbach, *ACS Appl. Mater. Interfaces* **2018**, *10*, 36910.
[5] K. N. Wood, M. Noked, N. P. Dasgupta, *ACS Energy Lett.* **2017**, *2*, 664.
[6] Y. Nishi, *J. Power Sources* **2001**, *100*, 101.
[7] A. C. Kozen, A. J. Pearse, C.-F. Lin, X. Han, M. Noked, M. A. Schroeder, S.-B. Lee, G. W. Rubloff, L. Hu, *ACS Nano* **2015**, *9*, 5884.
[8] Rosy, S. Akabayov, M. Leskes, M. Noked, *ACS Appl. Mater. Interfaces* **2018**, *10*, 29622.
[9] H. Cha, J. Kim, Y. Lee, J. Cho, M. Park, *Small* **2018**, *14*, 1.
[10] E. De La Llave, V. Borgel, K. J. Park, J. Y. Hwang, Y. K. Sun, P. Hartmann, F. F. Chesneau, D. Aurbach, *ACS Appl. Mater. Interfaces* **2016**, *8*, 1867.
[11] X. Xiang, K. Zhang, J. Chen, *Adv. Mater.* **2015**, *27*, 5343.
[12] G. Hu, L. Zeng, Z. Yang, Y. Jiang, Y. Yu, W. Li, L. Gu, X. Wei, F. Pan, M. Wang, *Adv. Energy Mater.* **2015**, *5*, 1402104.
[13] Y. Dong, S. Li, K. Zhao, C. Han, W. Chen, B. Wang, L. Wang, B. Xu, Q. Wei, L. Zhang, X. Xu, L. Mai, *Energy Environ. Sci.* **2015**, *8*, 1267.
[14] Y. Sun, Y. Lin, D. Zhang, M. Peng, D. Xia, G. Guo, L. Zheng, X. Wang, *Nano Energy* **2016**, *31*, 64.
[15] Q. Liu, D. Wang, X. Yang, N. Chen, C. Wang, X. Bie, Y. Wei, G. Chen, F. Du, *J. Mater. Chem. A* **2015**, *3*, 21478.
[16] F. Wang, S. W. Kim, D. H. Seo, K. Kang, L. Wang, D. Su, J. J. Vajo, J. Wang, J. Graetz, *Nat. Commun.* **2015**, *6*, 1.
[17] Y. Liu, X. Li, W. Shen, Y. Dai, W. Kou, W. Zheng, X. Jiang, G. He, *Small* **2019**, *1804737*, 1.
[18] A. Manthiram, X. Yu, *Small* **2015**, *11*, 2108.
[19] Z. Tong, R. Yang, S. Wu, D. Shen, T. Jiao, K. Zhang, W. Zhang, C. S. Lee, *Small* **2019**, *1901272*, 1.
[20] Q. Wang, C. Zhao, Y. Lu, Y. Li, Y. Zheng, Y. Qi, X. Rong, L. Jiang, X. Qi, Y. Shao, D. Pan, B. Li, Y. S. Hu, L. Chen, *Small* **2017**, *13*, 1.
[21] L. Yu, L. P. Wang, H. Liao, J. Wang, Z. Feng, O. Lev, J. S. C. Loo, M. T. Sougrati, Z. J. Xu, *Small* **2018**, *14*, 1.
[22] S. Zheng, G. Zhong, M. J. McDonald, Z. Gong, R. Liu, W. Wen, C. Yang, Y. Yang, *J. Mater. Chem. A* **2016**, *4*, 9054.
[23] K. Kaliyappan, J. Liu, B. Xiao, A. Lushington, R. Li, T. K. Sham, X. Sun, *Adv. Funct. Mater.* **2017**, *27*, 13.
[24] H. F. Wang, C. Tang, B. Wang, B. Q. Li, Q. Zhang, *Adv. Mater.* **2017**, *29*, 1.
[25] X. Xu, W. Liu, Y. Kim, J. Cho, *Nano Today* **2014**, *9*, 604.
[26] N. Zhang, X. Xiao, H. Pang, *Nanoscale Horiz.* **2018**, *4*, 99.
[27] D. Yang, J. Xu, X. Z. Liao, Y. S. He, H. Liu, Z. F. Ma, *Chem. Commun.* **2014**, *50*, 13377.
[28] A. Mukherjee, M. Banerjee, S. Basu, M. Pal, *AIP Conf. Proc.* **2014**.
[29] S. Hu, L. Scudiero, S. Ha, *Electrochim. Acta* **2012**, *83*, 354.
[30] N. Schumacher, K. Andersson, L. C. Grabow, M. Mavrikakis, *Surf. Sci.* **2008**, *602*, 702.
[31] M. Simões, S. Baranton, C. Coutanceau, *Appl. Catal. B* **2011**, *110*, 40.
[32] A. Serov, C. Kwak, *Appl. Catal. B* **2010**, *97*, 1.
[33] X. Zhong, Z. Yang, Y. Jiang, W. Li, L. Gu, Y. Yu, *ACS Appl. Mater. Interfaces* **2016**, *8*, 32360.
[34] W. Song, H. Hou, Z. Wu, X. Ji, K. Ye, Y. Zhu, M. Jing, C. E. Banks, J. Chen, *Phys. Chem. Chem. Phys.* **2015**, *17*, 159.
[35] W. Liu, H. Yi, Q. Zheng, X. Li, H. Zhang, *J. Mater. Chem. A* **2017**, *5*, 10928.
[36] R. A. Shakoor, D. H. Seo, H. Kim, Y. U. Park, J. Kim, S. W. Kim, H. Gwon, S. Lee, K. Kang, *J. Mater. Chem.* **2012**, *22*, 20535.
[37] Y. Qi, L. Mu, J. Zhao, Y. S. Hu, H. Liu, S. Dai, *J. Mater. Chem. A* **2016**, *4*, 7178.
[38] Q. Liu, X. Meng, Z. Wei, D. Wang, Y. Gao, Y. Wei, F. Du, G. Chen, *ACS Appl. Mater. Interfaces* **2016**, *8*, 31709.
[39] Y. Zhang, S. Guo, H. Xu, *J. Mater. Chem. A* **2018**, *6*, 4525.
[40] Y. Cai, X. Cao, Z. Luo, G. Fang, F. Liu, J. Zhou, A. Pan, S. Liang, *Adv. Sci.* **2018**, *5*, DOI 10.1002/advs.201800680.
[41] J. Sheng, P. Zhang, Q. Li, L. Zhou, Q. Wei, C. Xu, Y. Xu, Q. An, L. Mai, *Adv. Energy Mater.* **2016**, *6*, 1600389.
[42] Q. Liu, X. Meng, Z. Wei, D. Wang, Y. Gao, Y. Wei, F. Du, G. Chen, *ACS Appl. Mater. Interfaces* **2016**, *8*, 31709.
[43] M. Xu, L. Wang, X. Zhao, J. Song, H. Xie, Y. Lu, J. B. Goodenough, *Phys. Chem. Chem. Phys.* **2013**, *15*, 13032.
[44] M. Peng, B. Li, H. Yan, D. Zhang, X. Wang, D. Xia, G. Guo, *Angew. Chem. Int. Ed.* **2015**, *54*, 6452.
[45] H. S. H. Xiong, Y. Liu, Y. Yang, *J. Electrochem. Soc.* **2018**, *165*, A746.
[46] C. Shen, H. Long, G. Wang, W. Lu, L. Shao, K. Xie, *J. Mater. Chem. A* **2018**, *6*, 6007.
[47] P. R. Kumar, Y. H. Jung, J. E. Wang, D. K. Kim, *J. Power Sources* **2016**, *324*, 421.
[48] M. Banerjee, A. Mukherjee, A. Banerjee, D. Das, S. Basu, *New J. Chem.* **2017**, *41*, 10985.
[49] F. W. Y.-U. Park, J. Bai, L. Wang, G. Yoon, W. Zhang, H. Kim, S. Lee, S.-W. Kim, J. P. Looney, K. Kang, *J. Am. Chem. Soc.* **2017**, *139*, 12504.

[50] X. J. Weixin Song, X. Cao, Z. Wu, J. Chen, Y. Zhu, H. Hou, Q. Lan, *Langmuir* **2014**, *30*, 12438.

[51] H. Yang, X.-L. Wu, M.-H. Cao, Y.-G. Guo, *J. Phys. Chem. C* **2009**, *113*, 3345.

[52] Y. Xiao, S. Liu, F. Li, A. Zhang, J. Zhao, S. Fang, D. Jia, *Adv. Funct. Mater.* **2012**, *22*, 4052.

[53] G. Silversmit, D. Depla, H. Poelman, G. B. Marin, R. De Gryse, *J. Electron Spectrosc. Relat. Phenom.* **2004**, *135*, 167.

[54] A. Mukherjee, T. Sharabani, I. Perelshtein, M. Noked, *Batter. Supercaps* **2020**, *3*, 52.

[55] Y. Fang, L. Xiao, X. Ai, Y. Cao, H. Yang, *Adv. Mater.* **2015**, *27*, 5895.

[56] W. Song, X. Ji, Z. Wu, Y. Yang, Z. Zhou, F. Li, Q. Chen, C. E. Banks, *J. Power Sources* **2014**, *256*, 258.